Autonomous Medical Needle Steering In Vivo

Alan Kuntz[1], Maxwell Emerson[2], Tayfun Efe Ertop[2], Inbar Fried[3], Mengyu Fu[3], Janine Hoelscher[3], Margaret Rox[2], Jason Akulian[4], Erin A. Gillaspie[5], Yueh Z. Lee[6], Fabien Maldonado[5], Robert J. Webster III[2], Ron Alterovitz[3*]

[1]Kahlert School of Computing and Robotics Center, University of Utah; Salt Lake City, UT 84112, USA.

[2]Department of Mechanical Engineering, Vanderbilt University; Nashville, TN 37235, USA.

[3]Department of Computer Science, University of North Carolina at Chapel Hill; Chapel Hill, NC 27599, USA.

[4]Department of Medicine, Division of Pulmonary Diseases and Critical Care Medicine, University of North Carolina School of Medicine; Chapel Hill, NC 27599, USA.

[5]Department of Medicine and Thoracic Surgery, Vanderbilt University Medical Center; Nashville, TN 37232, USA.

[6]Department of Radiology, University of North Carolina School of Medicine; Chapel Hill, NC 27599, USA.

[*]Corresponding author. Email: ron@cs.unc.edu.

Abstract: The use of needles to access sites within organs is fundamental to many interventional medical procedures both for diagnosis and treatment. Safely and accurately navigating a needle through living tissue to a target is currently often challenging or infeasible due to the presence of anatomical obstacles, high levels of uncertainty, and natural tissue motion. Medical robots capable of automating needle-based procedures have the potential to overcome these challenges and enable enhanced patient care and safety. However, autonomous navigation of a needle around obstacles to a predefined target in vivo has not been shown. Here, we introduce a medical robot that autonomously navigates a needle through living tissue around anatomical obstacles to a target in vivo. Our system leverages a laser-patterned highly-flexible steerable nee-

dle capable of maneuvering along curvilinear trajectories. The autonomous robot accounts for anatomical obstacles, uncertainty in tissue/needle interaction, and respiratory motion using replanning and control and by utilizing safe insertion time windows. We apply the system to lung biopsy, which is critical for diagnosing lung cancer, the leading cause of cancer-related death in the United States. We demonstrated successful performance of our system in multiple in vivo porcine studies achieving targeting errors less than the radius of clinically-relevant lung nodules. We also demonstrated that our approach offers greater accuracy compared to a standard manual bronchoscopy technique. Our results show the feasibility and advantage of deploying autonomous steerable needle robots in living tissue and how these systems can extend the current capabilities of physicians to further improve patient care.

One-Sentence Summary: A medical robot autonomously steers a needle to targets in vivo, showing the clinical potential of automated needle steering.

INTRODUCTION

Access to targets inside organs is critical to many interventional medical procedures. Such procedures include biopsy, directed drug delivery, ablation, and localized radiation cancer treatment. These procedures are commonly performed throughout the body in organs such as the lungs, liver, prostate, and brain. Needles are a fundamental tool used in these procedures as they offer a minimally invasive method for traversing tissue en route to the target site (*1–6*). Safe and accurate navigation of a needle through living tissue to an intra-tissue target is currently often challenging or infeasible due to the presence of anatomical obstacles in the tissue, high levels of uncertainty, and natural tissue motion (for example, due to breathing). Medical robots capable of automating needle-based procedures in living tissue have the potential to overcome these challenges and enable an enhanced level of patient care and safety. However, automated navigation of a needle around obstacles to a predefined target in vivo has not been shown.

In this paper, we introduce a medical robot that autonomously inserts a needle in vivo to an intra-tissue target while navigating around obstacles. Our system leverages a flexible steerable needle, a type of needle capable of following curvilinear trajectories to avoid obstacles. This property enables steerable needles to reach regions in the anatomy that are otherwise inaccessible using rigid straight instruments (*7*), making them an appealing tool to overcome many of the challenges faced by existing needle insertion instruments. Precise manual insertion of steerable needles is challenging and unintuitive due to their non-holonomic constraints, making robotic autonomous actuation important (*8, 9*). Our group and others have put considerable effort into developing autonomous steerable needles and evaluating them via ex vivo and

benchtop experiments (*10–18*). Prior work has deployed steerable needles in vivo including via teleoperation (*8, 19*), but no prior in vivo work has reported deploying a steerable needle to a predefined target autonomously. Automating a steerable needle procedure in vivo is substantially more challenging than automating an insertion on a benchtop or in ex vivo tissues due to the higher stakes in obstacle avoidance (for example, puncturing a critical blood vessel can be fatal), the substantial increase in uncertainty in needle/tissue interaction properties, and the need to account for living tissue motion (for example, due to breathing).

The lung presents one of the most technically challenging applications for autonomous medical robots due to the pervasiveness of obstacles in the tissue and the continuous influence of respiratory motion. Diagnosing suspicious nodules in the lung parenchyma—the functional tissue of the organ—is an important medical problem since lung cancer, which is the annual leading cause of cancer-related death in the United States accounting for over 130,000 deaths each year, has a drastically more favorable outcome when diagnosed early (*20, 21*). Since nodules are generally small in the early stages of the disease, it is important for physicians to be able to accurately target small nodules, some just 8 mm in diameter (*22*). The current least invasive way to definitively diagnose lung nodules is via bronchoscopy, where a physician navigates an endoscope through the mouth and into the airways to a target site from which they insert a straight needle into the lung parenchyma. Although existing bronchoscopy techniques can accurately access targets near airways of sufficient diameter to accommodate the bronchoscope, they face accuracy challenges for more peripheral targets (those that are distant from the airways) stemming from respiratory motion and from the dense network of airways and vessels that present obstacles to deeper insertions (*23–25*). Combined with the small size of many clinically-relevant peripheral nodules, these limitations make existing tools insufficient for diagnosis in many cases.

In this work, we accomplish an intraparenchymal in vivo procedure via a steerable needle deployment in one of the most difficult organs—the lungs—overcoming challenges of employing medical robot autonomy inside a living, dynamic organ. We do this via a bronchoscopically-deployed robotic steerable needle that achieves high curvature through laser patterning and is deployed via an aiming device. Our system accounts for tissue and respiratory motion by using registration algorithms and defining safe insertion time windows during the breathing cycle during which the needle can safely advance. It accounts for anatomical obstacles, such as clinically-relevant vasculature, bronchi, and the visceral pleural boundary, via motion planning, and it accounts for uncertainty in tissue/needle interaction and intra-operative physician choices with replanning and control. The system includes a user interface that visualizes the status of the procedure and supports autonomous steerable needle deployment.

Prior work on needle steering for this lung medical application (*26–28*) did not consider the challenges of in vivo targeting, focusing experiments solely on stationary ex vivo tissue, without consideration of respiratory motion. Furthermore, targets were selected manually and there was no teleoperated aiming device or re-planning prior to autonomous needle insertion to compensate for imprecise human actions and other unmodeled effects. There also was no user interface with which the physician could monitor procedure progress, receive cues for cor-

recting their initial needle placement, or monitor the actions of the robotic system. Through our advancements to enable accurate steerable needle deployment in vivo, we are able to overcome the challenges of existing diagnostic bronchoscopy techniques to accurately reach even the smallest clinically-relevant nodules in previously hard-to-reach areas of the lung.

Through in vivo porcine experiments, we show the clinical feasibility of our system and demonstrate successful in vivo autonomous obstacle-avoiding needle insertions to randomly specified intra-tissue targets. We then show our system's ability to outperform an existing clinical approach in accessing peripheral regions of the lung by conducting a study comparing our system to an endobronchial technique used in modern clinical care. Through this study, we also demonstrate the benefits of automation for the application of endobronchial intraparenchymal needle biopsy. Our results demonstrate that autonomous steerable needle robots can succeed in the realistic setting of a living mammal, and that automation can enable physicians to leverage robotic tools to achieve otherwise challenging manual tasks. Our system has the potential to enable early diagnosis for more patients with lung nodules, and could be generalized to advance the capabilities of physicians in other medical procedures throughout the body.

RESULTS

Semi-autonomous steerable needle system overview

Our system consisted of three stages, each of which corresponded directly to a portion of the medical procedure (Fig. 1). A preoperative CT scan of the patient (which in our experiments corresponded to an in vivo or ex vivo porcine model) was used to segment the anatomical environment, including obstacles, which was used to inform the three stages. Stage 1 consisted of a traditional bronchoscope, augmented with a 6-DOF electromagnetic tracking coil attached to its distal tip, that was inserted through the mouth of the patient and into the airways by a physician (which in our experiments was either an interventional pulmonologist or other expert). The physician navigated the bronchoscope inside the airways to a position from which subsequent stages of the system could be deployed to reach the target. This portion of the procedure was performed manually, leveraging the experience of the physician in bronchoscope navigation. Stage 2 consisted of a teleoperated aiming device that the physician passed through the working channel of the bronchoscope following navigation. The aiming device was a tendon-actuated beveled nitinol tube laser-patterned to increase its achievable levels of curvature (*29*). The aiming device enabled the physician to reorient the steerable needle with respect to the target in the parenchyma prior to autonomous needle deployment. This was an important step in successfully transferring control from the physician (who navigated the bronchoscope) to the robot (that will autonomously steer the needle to the target) as it enabled the physician to correct deviations in the current needle pose from the planned start pose. Stage 3 consisted of a steerable needle (*26*) which was passed through the working channel of the bronchoscope and through the aiming device. The needle was highly flexible and featured a bevel tip, which caused it to curve in the direction of the bevel when inserted into parenchymal tissue. The needle's direc-

tion of curving could be changed by reorienting its bevel tip by axially twisting the needle at its proximal end. The needle was laser-patterned to achieve high curvature in soft, inflated lung tissue (*26*). A 5-DOF tracking coil was embedded within the needle at its distal tip. The robot autonomously deployed the needle along a planned trajectory under closed-loop control to the target while avoiding obstacles (*12, 27*). The robot steered the needle autonomously to overcome the known challenges of manual deployment of steerable needles (*8, 9*). The three stages' control methods—manual, teleoperation, and autonomous—harnessed the respective strengths of the human and robot, with bronchoscope navigation relying on the physician's existing expertise, the teleoperated aiming device serving as a bridge between manual control and robotic automation, and the final stage leveraging the robot's capabilities to autonomously maneuver the steerable needle accurately to the target.

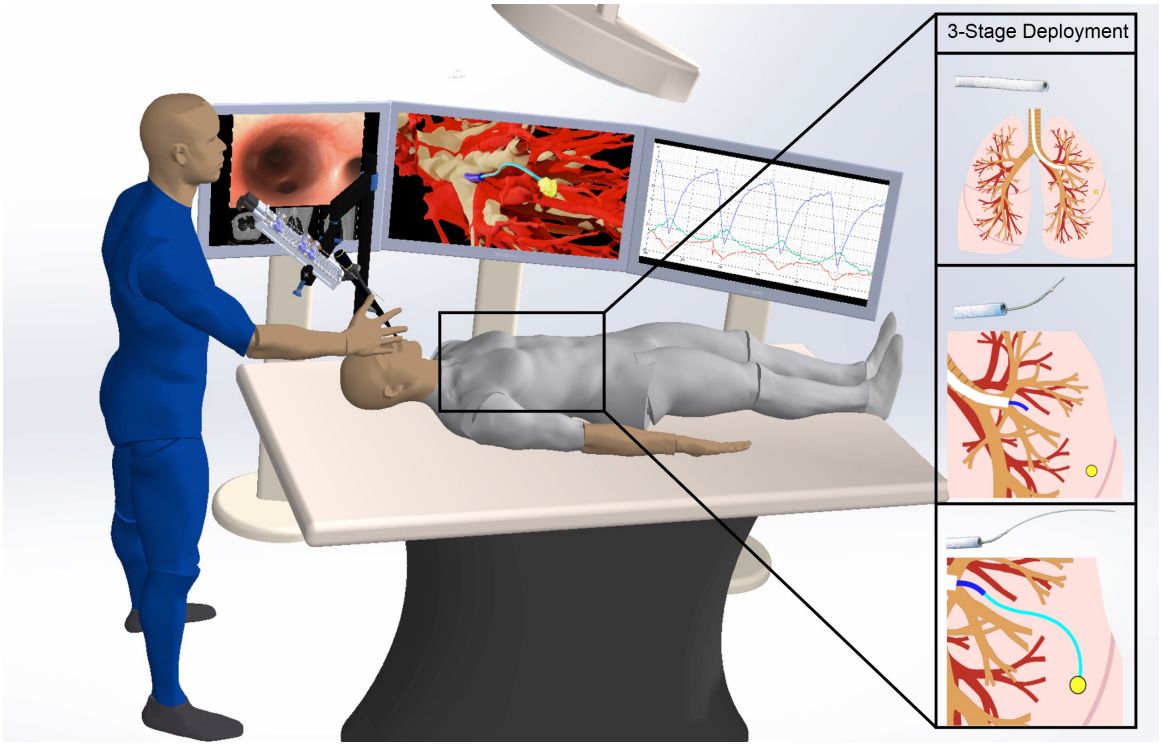

Fig. 1: Overview of the semi-autonomous medical robot's three stages in the lungs. Stage 1 consists of a physician manually navigating a traditional bronchoscope through the airways. Stage 2 consists of a physician teleoperating the aiming device. Stage 3 consists of autonomous needle deployment through the parenchyma to the nodule while accounting for respiratory motion and avoiding anatomical obstacles such as clinically-relevant vasculature, bronchi, and the visceral pleural boundary.

Workflow of the system deployment

Our system was designed to enable accurate access to clinically-relevant lung nodules. The workflow of a procedure, as shown in Fig. 2, consisted of creating a geometric model of the patient's anatomy, planning the deployment of each of the three stages via motion planning, and finally executing the plan via manual control, teleoperation, and automation.

In the pre-operative phase, we acquired a CT scan of the patient's chest under an inspiratory breath hold. The breath hold, commonly utilized for imaging and other clinical procedures such as targeted radiation therapy (*30*), performs two important functions. First, it reduces motion artifacts in the scan from natural tissue motion, and second, it captures a state of the environment that we can accurately return to with subsequent breath holds. Performing the breath hold at inspiration, when the lung is expanded, provided us with the most detailed view of the anatomy. Pre-operative CT scans in clinical practice are typically performed at inspiration for this same reason. We then segmented the CT scan using an automatic segmentation algorithm (*31*). This provided us with a three-dimensional representation of the underlying patient anatomy, including the bronchial tree, blood vessels, and pleural boundary. We used the segmentations to specify the planning environment for the motion planner, including the free workspace and obstacles. In our experiments, we randomly sampled a target at this stage to mimic a clinical procedure, in which the target nodule would be identified in the pre-operative scan. For a given target in the lung parenchyma, we used our motion planning algorithm to generate 3 - 5 candidate plans, each plan composed of a motion plan for each of the three stages (*12*). Each plan has a cost that considers proximity to obstacles. The candidate plans were overlaid in the segmented anatomy and displayed to the physician in the user interface. The physician then chose one of these plans, combining the results of the motion planner with their own clinical knowledge and preferences.

Prior to bronchoscope navigation, we performed registration using sensorized fiducials that are attached to the exterior chest wall of the patient. We improved this registration by driving the bronchoscope through the airways and collecting a point-cloud of the airway's medial axis in the electromagnetic tracker frame. We performed a point-cloud registration between the set of collected points and the skeleton of the segmented bronchial tree using the iterative closest point (ICP) algorithm (*32*). This additional registration step is particularly important in vivo as it helps account for internal tissue deformation that the fiducials on the chest wall, given their distance from the lung, are not able to accurately capture. Throughout the procedure, the poses (positions and orientations) of the bronchoscope and steerable needle were tracked in real-time using an electromagnetic (EM) tracking system (Aurora, Northern Digital, Inc.). The poses were overlaid in the anatomy using the registration transformation and displayed to the physician via the user interface.

Next the physician began the system deployment. The physician first manually navigated the bronchoscope based on the three-stage plan they selected. Next, the physician pierced into the lung parenchyma using a piercing stylet deployed through the working channel of the bronchoscope. The physician then inserted the aiming device through the working channel, which

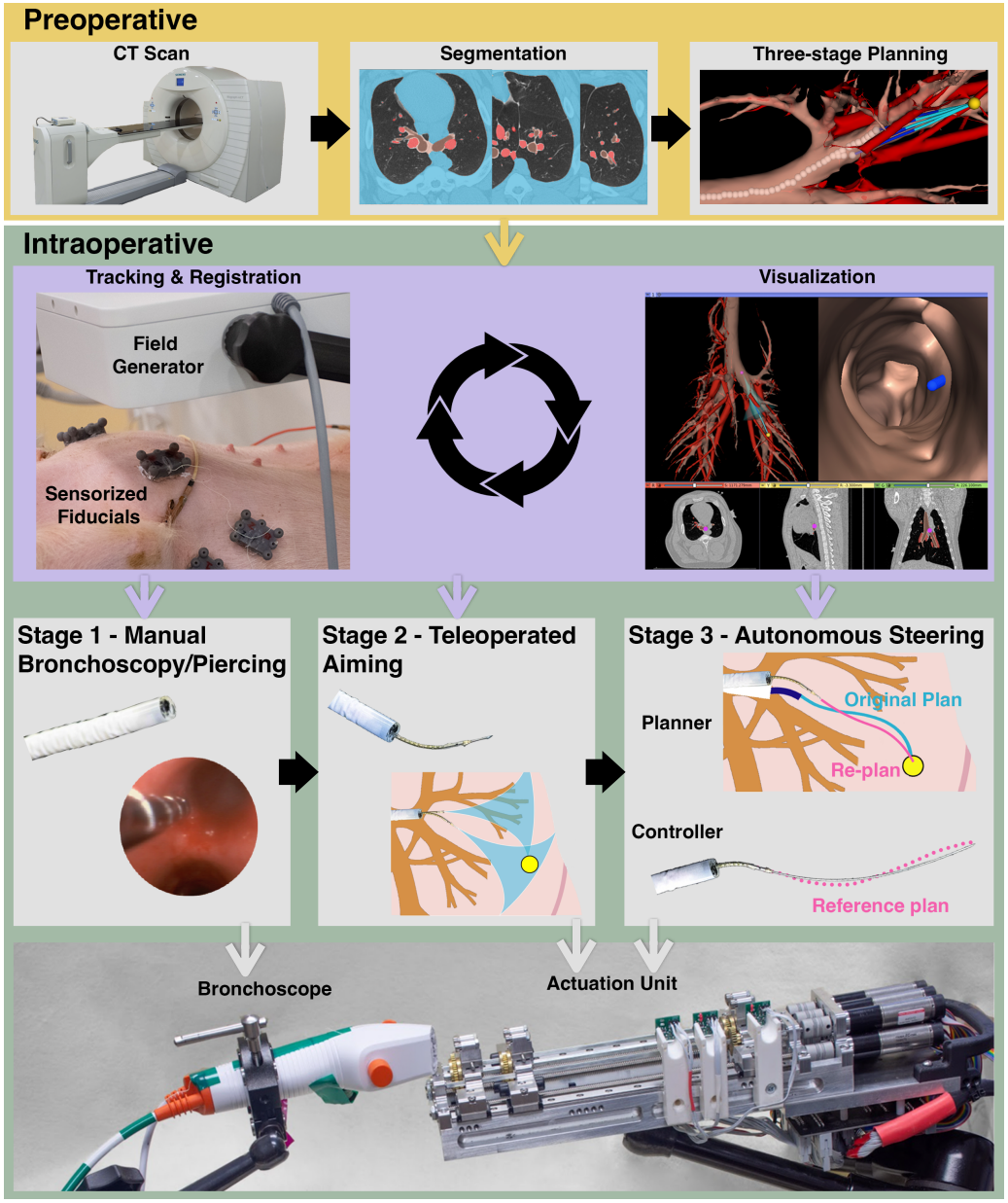

Fig. 2: Workflow of the procedure showing the integration of the software and hardware components. We show both the procedure sequence flow (thick black arrows) and information flow (thin colored arrows). A CT scan is segmented and used to construct a map leveraged by the 3-stage motion planning software in the preoperative phase. The scan, segmentation, and 3-stage plan are used intraoperatively in the procedure, during which the devices are tracked, registered to the CT-frame, and visualized for the operator. These steps inform the 3-stage deployment of the system and the interaction between the physician and the robot.

was passed into the parenchyma over the piercing stylet. The piercing stylet was then removed and replaced with the steerable needle. If any error occurred in the manual deployment that resulted in deviation from the planned trajectory, either from operator error or tissue deformation, the system directed the physician to adjust the position and orientation of the steerable needle to best align with the target. This was done by teleoperating the aiming device. The system automatically indicated to the physician in the user interface when the realignment was successful. Once the physician reoriented the steerable needle toward the target, the system recomputed an obstacle-free motion plan for the needle in the parenchyma to the target, accounting for the current start pose of the needle. The system automatically selected the safest plan that maximized distance to obstacles along the entire length of the planned needle insertion. The robot then, over a sequence of several breath holds, autonomously steered the needle along the planned trajectory to the desired target. With the exception of minor differences described in the Methods section, this workflow was used for both the in vivo and ex vivo experiments.

Needle steering under respiratory motion

The lungs deform during breathing, displacing the parenchyma and the anatomy embedded within. This leads to a discrepancy between the preoperative segmentation of the anatomy and the intraoperative state of the anatomy. To account for this change in the environment and achieve in vivo needle steering in the lung while avoiding obstacles, we defined safe insertion time windows during the breathing cycle when the needle can safely advance. Specifically, we monitored the respiratory cycle using the fiducials attached to the exterior chest wall by plotting the displacement of the fiducials over time. We defined the start of the safe insertion time window as the phase of the breathing cycle corresponding to peak tidal volume (a state of inspiration). We selected this as the start of the time window for three reasons. First, as mentioned earlier, the CT scan used for procedure planning and segmentation in clinical practice is typically acquired in a state of inspiration, which provides the most detailed view of the target and anatomical obstacles. Second, compared with other phases of the breathing cycle, during peak tidal volume the lung is most expanded, meaning that there is more free space for steering the needle (Fig. 3A). Third, peak tidal volume represents a discrete state of the lung that is easy to repeat. At the start of the safe insertion time window, we initiated a breath hold and the robot began steering the needle. After a brief breath hold, the safe insertion time window ended and the robot paused insertion of the needle. The breathing cycle then continued normally without the robot actuating the needle, and we required at least two normal breathing cycles before initiating another breath hold. Since insertion of the steerable needle required more time than a single safe insertion time window allowed, we repeated the process each time the breathing cycle re-entered a safe insertion time window until the needle reached the target.

To define the duration of the safe insertion time window, we studied the effect of varying the duration during an in vivo study. A series of short breath holds is preferable to a long breath hold for the overall physiologic stability of the animal, and also is beneficial for reducing undesirable tissue motion. The ability of the animal and ventilator to maintain a breath

hold decreases over time, leading to a steady deflation. This could be seen by monitoring the displacement of the chest markers from their position at the initiation of the breath hold over a single long, approximately 40-second, breath hold (Fig. 3B). Performing a similar analysis but using a sequence of short, approximately 10-second, breath holds reduced the magnitude

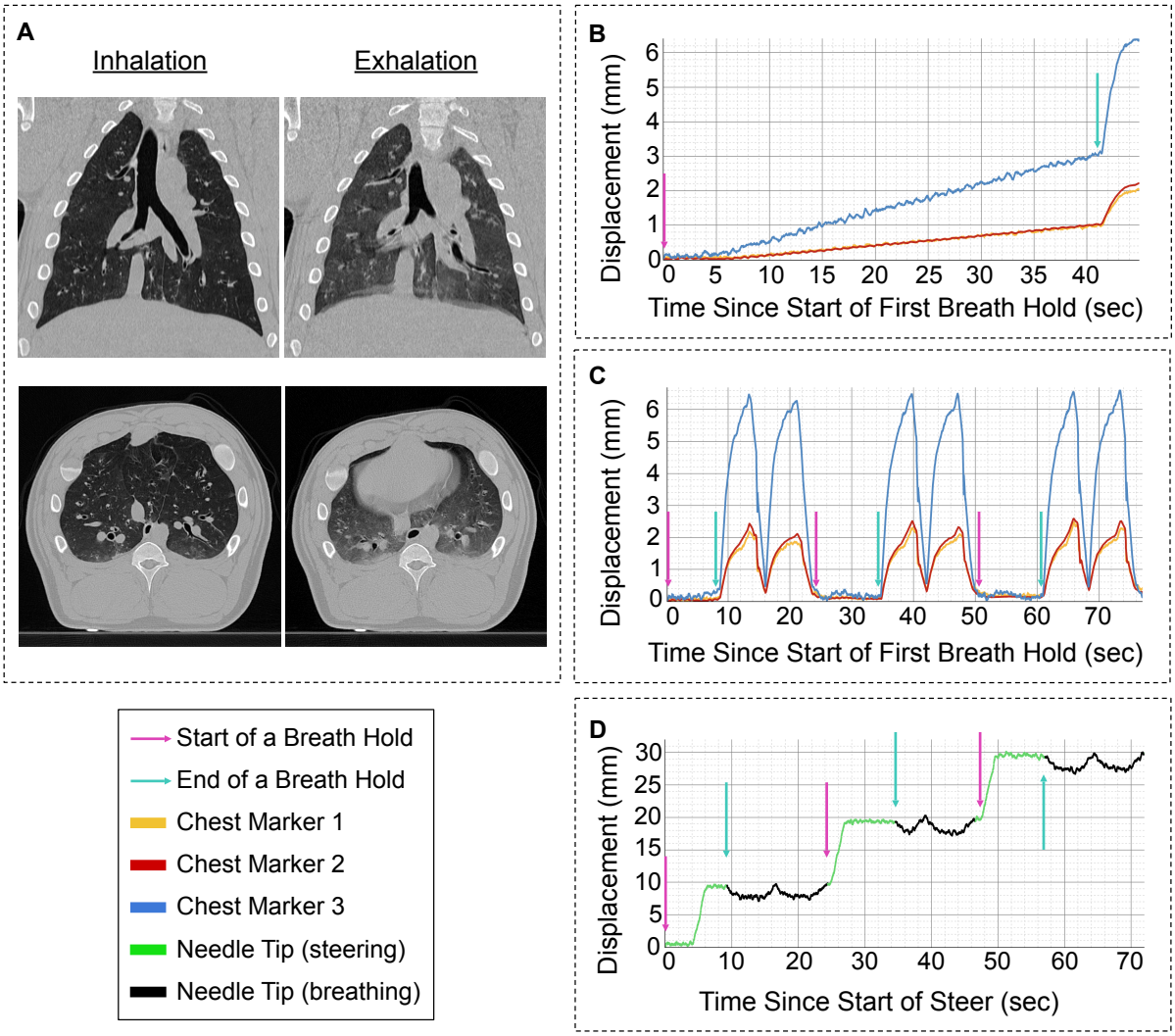

Fig. 3: Effect of respiratory motion on the procedure. (**A**) Transverse and coronal views from CT scans taken at peak tidal volume and at functional residual capacity (end-inspiration and end-expiration, respectively). (**B**) Chest marker displacement over a single long breath hold (breath hold stops at approximately 40 seconds). (**C**) Chest marker displacement over a sequence of short breath holds, where the displacements remain under 1mm during approximately 10-second breath holds and rise substantially only between the breath holds. (**D**) Displacement of the needle during one of the in vivo deployments.

of the deflation as measured by the displacement of the markers from their initial position at the beginning of the first breath hold (Fig. 3C). By only requiring short breath holds, we were better able to ensure that any needle motion in the tissue is planned and caused by the robot and not a result of natural tissue motion. Combined with the delay in deflation, this enabled us to achieve a consistent lung state for the duration of each segment of steering and globally across segments for the entire steer. Based on a 10-second safe insertion time window, our system divided the planned needle trajectory into sequential trajectories with arclengths of 10 mm and the beginning of each of these trajectory segments was synchronized with the beginning of a breath hold (Fig. 3D). The robot then inserted another trajectory segment in each safe insertion time window until the trajectory was completely executed.

In vivo intraparenchymal needle steering in lung

Prior work by us and others has demonstrated ex vivo needle steering in lung tissue, as well as other organs (*1, 3, 26, 27*). These experiments are important for characterizing the properties and capabilities of the devices, but are insufficient to indicate their clinical feasibility. This is due to the major differences between in vivo and ex vivo environments including respiratory motion, tangible medical risks, and higher levels of uncertainty in the procedure. These differences are especially prominent in the lungs—an organ under constant physiological motion. Leveraging a porcine model, commonly used in research due to its similarity in size and structure to human chest anatomy (*33*), we evaluated our system's performance in a realistic setting and demonstrated its clinical potential via in vivo porcine experiments (Fig. 4).

We performed three deployments of our system in two live animals (102 kg and 42 kg). Prior to each system deployment, we randomly sampled a target in the lung parenchyma from the initial CT scan that was used for segmenting the anatomy. The final error for each steer was calculated in the EM tracker space and was measured using the Euclidean distance between the tracking coil at the needle tip and the target. The first procedure was performed in the left lung lobe of the first animal with an overall steerable needle trajectory length of 43 mm. The final error at the target was 3.49 mm. The second procedure was performed in the right lung lobe of the first animal with an overall steerable needle trajectory length of 48 mm. The final error at the target was 1.81 mm. The third procedure was performed in the left lung lobe of the second animal with an overall steerable needle trajectory length of 38 mm and with a final targeting error of 2.72 mm. The quantitative metrics of the three deployments are visualized in Fig. 4B, with a United States one-cent coin (9.53mm radius) as a scale reference to better illustrate the small magnitude of the targeting errors. The planned and tracked trajectories of the three steers are shown in Fig. 4C. The black segments in the tracked points represent the needle motion during normal tidal breathing in between sequential breath holds. These plots demonstrate that the needle was able to return to the same position over each period of tidal breathing between the sequence of short breath holds. The success of the system for the three steers is further depicted in Fig. 4D, showing the magnitude of the trajectory error over time where trajectory error is measured as the Euclidean difference between paired points in the tracked and planned needle

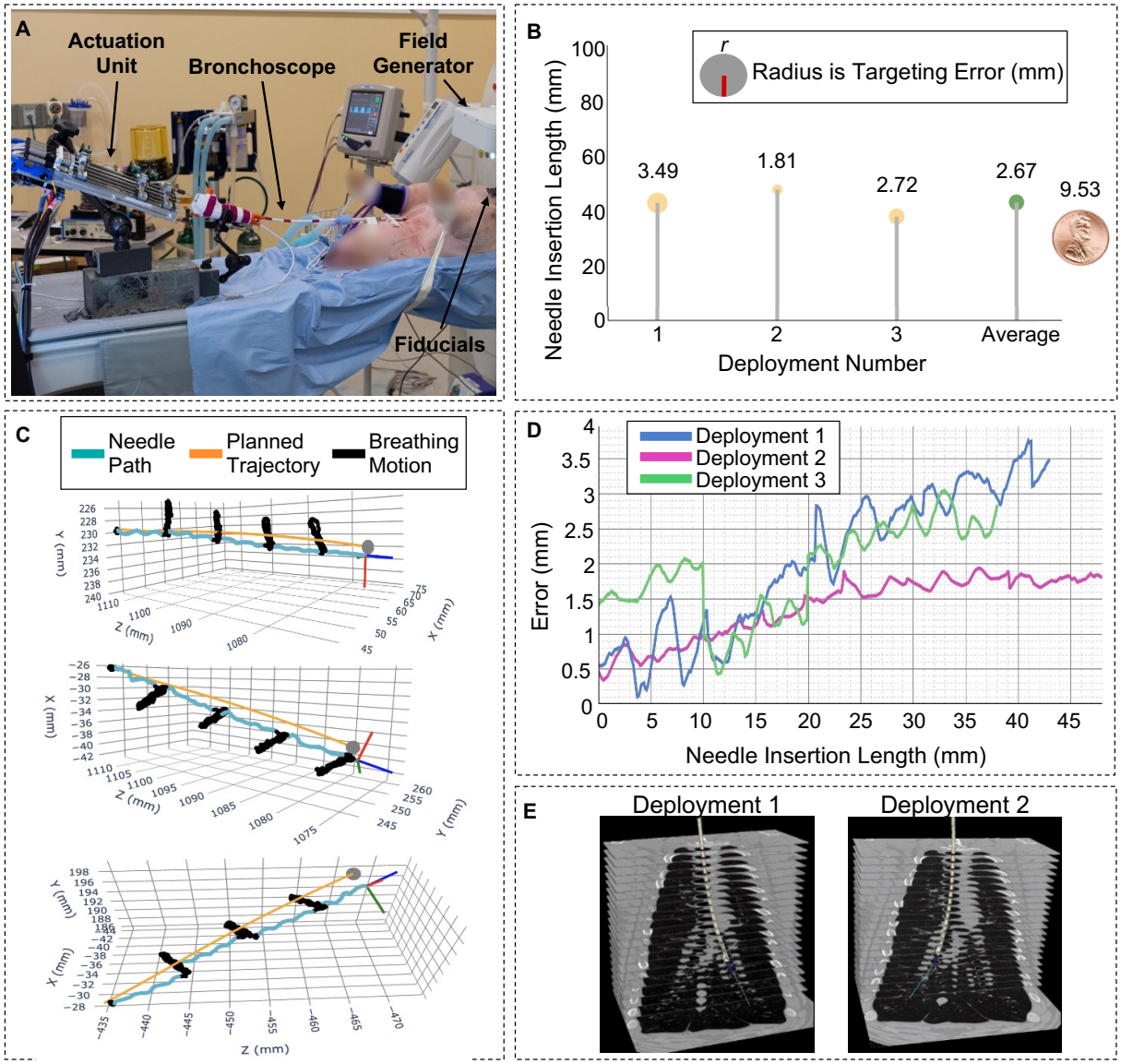

Fig. 4: In vivo porcine lung results. (**A**) The in vivo experimental setup. (**B**) Results for all system deployments with needle steer length on the y-axis, steer number on the x-axis, and a circle with radius equal to the targeting error. The penny is for scale. (**C**) Planned and tracked needle trajectories. (**D**) Magnitude of the trajectory error for each deployment. (**E**) Visualization of the deployments shown within slices of the CT scan of the anatomy.

trajectory. The targeting errors of the three deployments in vivo are consistent in magnitude with the targeting errors achieved in ex vivo system deployments during the comparison study described below.

Following each procedure, a physician confirmed the safety of our system by closely exam-

ining the post-deployment CT scan. The autonomous steerable needle did not collide with any anatomical obstacles in any of the procedures. Notably, there were no adverse events including pneumothorax, atelectasis, or vessel perforation and hemorrhaging.

Comparison with manual clinical bronchoscopy

To evaluate our system's ability to improve access to hard-to-reach peripheral targets, we conducted a study in ex vivo porcine lung comparing our system to a modern diagnostic bronchoscopy technique. For the manual diagnostic bronchoscopy, two expert interventional pulmonologists navigated a clinical bronchoscope (Ambu) with electromagnetic navigation and CT guidance. Electromagnetic navigation was provided by embedding an electromagnetic sensor at the distal tip of the bronchoscope and visualizing the real-time pose of the bronchoscope in our visualization software registered to the segmented anatomy. The study was performed in a CT scanner room, which provided the physicians the opportunity to utilize the scanner for localization confirmation throughout the procedure. Following navigation of the bronchoscope,

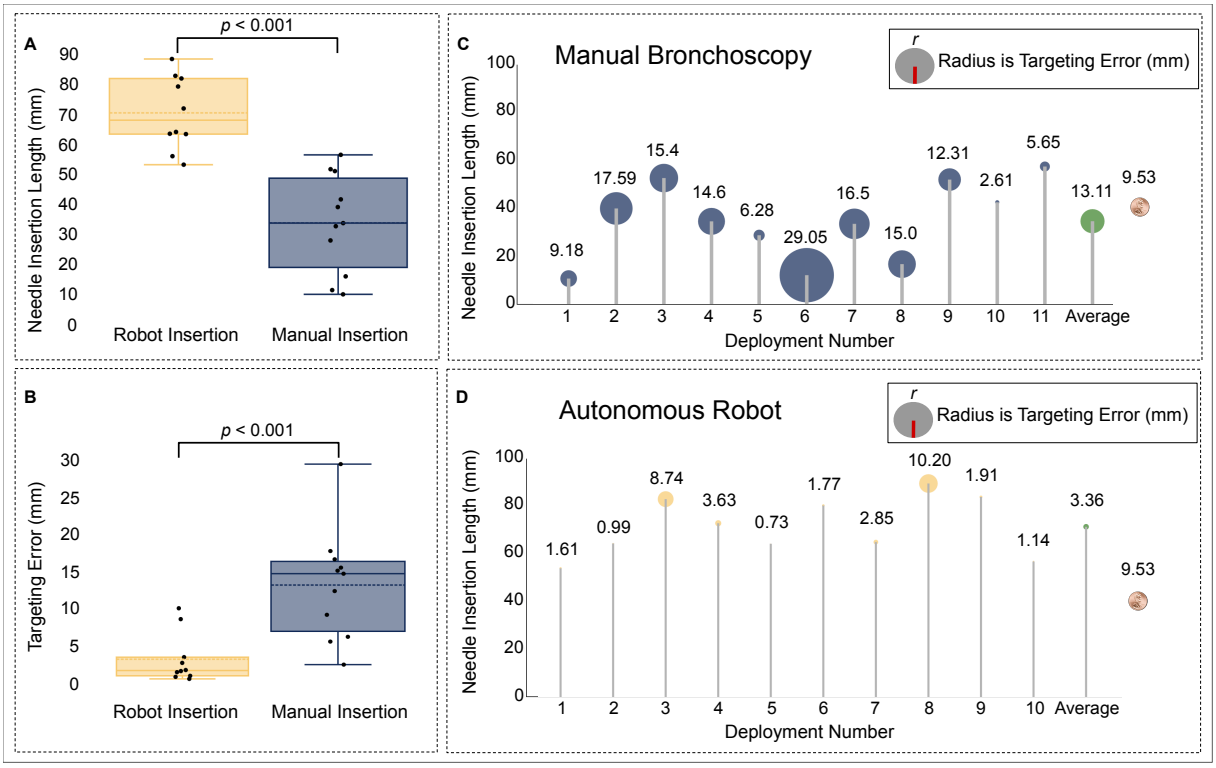

Fig. 5: Results from the comparison experiments between the manual bronchoscopy and the proposed robotic system. (**A**) Deployment lengths. (**B**) Targeting errors. (**C**) Results from the manual bronchoscopy deployments. (**D**) Results from the robotic steerable needle deployments.

the physician inserted a straight needle with an electromagnetic sensor embedded at its tip toward the target. The stiffness of the straight needle was consistent with stiffness properties of existing clinical biopsy tools used in bronchoscopy. For the robotic system, an engineer experienced with the system performed the deployments. The engineer was provided the same electromagnetic navigation and visualization during the bronchoscope navigation as was given to the physicians in the clinical bronchoscopy cases.

To assess the ability of each approach to accurately access peripheral targets, we randomly sampled virtual targets in the segmented anatomy from peripheral regions of the ex vivo lungs. The measured outcomes included the insertion length of the devices in the lung parenchyma and the targeting error. Targeting error was measured as the Euclidean distance between the tracked needle tip and the target.

We performed 11 deployments of the clinical bronchoscopy in 5 unique lungs, and 10 deployments of the robot system in 6 unique lungs. The distribution of the needle insertion lengths and the targeting errors for our system and the clinical bronchoscopy are shown in Fig. 5A and Fig. 5B, respectively. The average needle insertion length when using the robot system was longer than the average needle insertion length when performing the clinical bronchoscopy (70.75 mm $\pm$ 11.49 mm and 34.23 mm $\pm$ 15.44 mm, respectively, $p = 0.000013$). The targeting error for the robot deployments was substantially lower than that for the clinical bronchoscopy (3.36 mm $\pm$ 3.18 mm and 13.11 mm $\pm$ 6.91 mm, respectively, $p = 0.0009$). The needle insertion length and targeting error of each individual deployment are shown in Fig. 5C, with a United States one-cent coin as a reference scale for the magnitude of the targeting errors. The ability of the steerable needle to achieve curvilinear trajectories and avoid anatomical obstacles is shown in Fig. 6.

During the experiments, we observed that the physician preferred to drive the bronchoscope further into the airway to enter the parenchyma at a more distal point compared with the more proximal insertion recommendations computed by the motion planner for the robot. The physician's intention was to enter the parenchyma at a point closest to the target, but given the decreasing diameter of the airways, this restricted the range for angling the bronchoscope's distal tip. By exiting the airway at a more proximal site, our system provided more actuation and better orientation positioning for the bronchoscope navigation. We also noticed that the physician-guided needle insertions were on average of greater length than existing clinical practice, likely reflecting the high risk tolerance of the physician in a non-clinical setting. Since manual needle insertion is not explicitly planned with respect to obstacles in the environment in current clinical practice, most clinical tools are limited to 20 - 30 mm of insertion (*34, 35*). Our system is able to access more peripheral targets via autonomous needle steering by explicitly computing an obstacle-free trajectory in the parenchyma and following it under closed-loop robotic control.

These results demonstrate our system's ability to reach peripheral intraparenchymal targets in the lung, which are challenging for existing bronchoscopic techniques, with high accuracy.

DISCUSSION

In this work, we demonstrated autonomous intraparenchymal needle steering to a target in the highly challenging and uncertain environment of in vivo lungs. We achieved this using a bronchoscopically-deployed robotic steerable needle that achieves high curvature through laser patterning and is deployed via an aiming device. We accounted for tissue and respiratory motion by using registration algorithms and defining safe insertion time windows during the breathing cycle during which the needle can safely advance. We accounted for anatomical obstacles via motion planning and accounted for uncertainty in tissue/needle interaction and intra-operative physician choices with replanning and control. The system's user interface displays real-time tracking in a segmented view of the anatomy and supports autonomous steerable needle deployment. No prior autonomous medical robot has completed a task in an obstacle-cluttered parenchyma of an organ where visual supervision is not possible and an implicit roadmap of the anatomy, such as the lumen of a blood vessel, does not exist (*6, 36–40*). Prior work on needle steering in vivo focused on measuring needle/tissue interaction properties or teleoperation without automatic consideration of patient-specific obstacles (*8, 19, 41*). We demonstrated the clinical feasibility of our semi-autonomous system through in vivo porcine experiments and through a comparative study where our system outperformed a modern clinical approach in safely and accurately accessing hard-to-reach peripheral intraprenchymal targets. The results of the comparative study also highlight the benefits of automation for lung nodule biopsy, enabling our system to leverage steerable needles to safely traverse the lung parenchyma. Automating

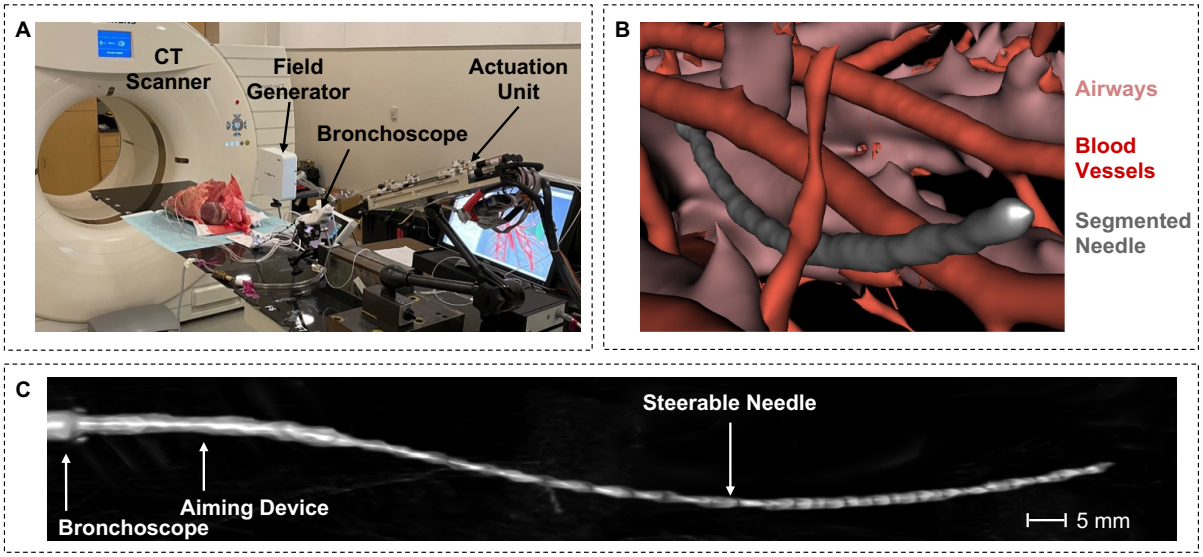

Fig. 6: Capabilities of the flexible steerable needle. (**A**) The ex vivo experimental setup. (**B**) Segmentation of the steerable needle following deployment in ex vivo lungs. (**C**) The 3D rendering of the steerable needle corresponding to the segmentations.

medical procedures and subtasks has the potential to standardize patient care independently of the natural variation in inter-physician and intra-physician performance while also refocusing the time of expert physicians to higher level tasks.

The results of our experiments indicate that steerable needles could enable physicians to access targets in the lung for diagnosis or treatment that are beyond the safe reach of existing tools. By integrating our robotic system with a conventional bronchoscope, we limit the additional training required to operate our system, which will facilitate its availability to patients without access to highly sub-specialized physicians or tertiary care centers. The decoupling of the robotic steerable needle system from the bronchoscope makes it so that our system could be used with any bronchoscope, including robotic bronchoscopy systems, with a sufficient working channel.

The system and results presented in this work highlight the clinical potential of steerable needles, enabling physicians to safely access regions in living soft tissue while avoiding obstacles. Given our success in the highly challenging environment of the lung, we envision that the third stage of our system, the autonomous steerable needle robot, could be useful in other clinical applications where steerable needles have been proposed, including drug delivery, brachytherapy, ablation, and biopsy in the brain, prostate, and liver (*3, 5, 42, 43*).

The density of obstacles in the lungs makes this application technically challenging and highlights the importance of a system like the one we present that integrates motion planning, steerable needles, and automation to account for obstacles. For example, in a post-procedure analysis of the in vivo lung images, we randomly sampled 100 points per lung along the airway walls that are bronchoscopically accessible and discovered the samples are on average just 3 mm away from a blood vessel obstacle. Similarly, the targets we deployed to in vivo were on average 7.3 mm from the nearest obstacle. And as the field of medical image segmentation advances with new deep learning models capable of accurately segmenting ever finer structures, we will be able to directly incorporate these new segmentation advancements to enable our system to avoid less critical but potentially relevant smaller obstacles.

Building on the success of the system, there are areas for development to further improve the system's performance. The characteristics of the steerable needle that we use in our experiments were empirically determined via iterative experimentation. Although the laser pattern we use enables the needle to achieve a high level of curvature, we did not perform an optimization analysis of this pattern. By performing such an analysis, we would be able to tune the laser pattern on the needle specifically for inflated lung tissue thereby increasing the workspace and error compensation capabilities of the steerable needle. The curvature capabilities of the steerable needle might be even further enhanced by exploring new strategies like magnetically actuated steering (*44*). Although we have implemented methods such as re-planning and closed-loop control to overcome noise in the procedure, our system does not explicitly model and account for all sources of noise. In future work, we could create models of the effect of heartbeat on needle motion and integrate online models of needle curvature estimation to account for natural variation (*45*). New needle designs combined with planners and controllers that consider more patient-specific modeling beyond anatomy could enable the system to further improve accuracy

in reaching the target.

Motivated by the benefits of automating the steerable needle as shown through the comparative study, we plan to automate the teleoperated aiming device in future work to autonomously correct for deviations in the piercing location from the planned exit point (Fig. S1). Also, although the porcine model is an excellent translational model for respiratory medicine, the anatomy of the porcine lung differs in a couple meaningful ways from the anatomy of human lungs. These differences include a monopodial branching structure of the airways compared to the bipodial structure of human airways, large blood vessels that run adjacent to the main airway branch bilaterally making it more challenging to pierce into the parenchyma in porcine lungs, and an absence of the pores of Kohn which prevent collateral ventilation in porcine lungs and result in more atelectasis (*33, 46*). All of these anatomical differences make the porcine anatomy a more challenging procedural environment than human anatomy, and the next step in this research is to assess the performance of our system in a human cadaver followed by live human trials.

Our results demonstrate the potential for improved medical outcomes, specifically in early lung cancer diagnosis, when using medical robots with autonomous capabilities. These results highlight the increasing need for determining appropriate certification processes and regulatory pathways for autonomous medical robots to be approved and adopted for clinical use. Regulatory frameworks that have been developed and used for autonomous systems in other industries in which safety is critical, such as the approval processes by the Federal Aviation Administration (FAA) for flight automation systems on commercial airplanes, could be helpful in guiding such efforts. However, medicine is unique from other autonomous system applications in many consequential ways, particularly due to the broad diversity of tasks, environments, sensors, risk factors, and ethical considerations that arise in surgical and interventional medical procedures (*47*). Appropriate regulatory processes should ensure legal and safe deployment of autonomous medical robots in human cases to provide high quality patient care and establish confidence in such systems by the general public.

MATERIALS AND METHODS

Steerable needle robotic platform

The steerable needle is made from a superelastic nitinol tube with 0.69 mm outer diameter (OD) and 0.53 mm inner diameter (ID). To increase the curvature capabilities of the needle, we laser pattern the approximately 11 cm distal-most section of the needle using a continuous helical puzzle piece pattern with a helix angle of 35° (*26*). To track the needle intra-operatively, we place a 5DOF magnetic tracking coil with 0.41 mm diameter and 4.9 mm length (Northern Digital Inc.) at the tip of the needle and glue it in place with cyanoacrylate adhesive. To construct the aiming device, we laser cut the notched design presented in (*29*) at the distal section of a 1.5 mm OD and 1.3 mm ID superelastic nitinol tube. We attach a 40 lb microfilament braided line (PowerPro) to the distal tip of the aiming device and use the line as a tendon to actuate the

aiming device from the proximal end of the tube. Both the needle and the aiming device are deployed through a disposable clinical bronchoscope that has a 5.5 mm OD at its widest section, and a 2.2 mm ID working channel that is 60 cm in length (Ambu aScope, Regular). We place a 6DOF magnetic tracking coil with 0.8 mm diameter and 9 mm length (Northern Digital Inc.) at the distal end of the bronchoscope to allow us to track the bronchoscope intra-operatively.

The needle actuation unit consists of three carriages: two for independently controlling translation and rotation of the aiming device and the flexure-tip steerable needle, as well as a third carriage for actuating the pull-wire of the aiming device. These carriages travel along lead screws driven by motors at the base of the unit that are controlled by custom electronics boards. The system features a quick-loading tube carriage concept, where each tube in the system has a driven gear that snaps into place via holding arms and engages with a driving gear on the carriage, enabling the physician to easily switch between tools if necessary (*2*).

Fiducial Registration

To register between the electromagnetic field generator frame and the CT scanner frame, we utilize 3D printed fiducials that are placed on the outer surface of the lungs in ex vivo experiments and on the chest wall for in vivo experiments. The fiducials are rigid plastic markers with a geometry that includes seven spheres. In each fiducial we embed a 6 DOF electromagnetic tracking coil. Each fiducial is pre-calibrated prior to the experiment such that the center of each sphere is known relative to the embedded tracking coil. This is done by placing a probe in the center of each sphere (into a divot designed to the size of the probe tip) while the location of the central tracker is also recorded. The spheres of every fiducial are easily recognizable in CT image space. As such, we manually segment the location of the sphere centers for each fiducial from the preoperative CT scan. Then, given the known point-to-point correspondence between the EM tracked sphere centers and the sphere centers in the CT scan, we utilize a registration algorithm (*48*) to line up the CT image space with the magnetic tracking space.

Tree-to-Tree Registration

To improve the registration, we refine the fiducial registration using the correspondence-free iterative closest point (ICP) registration method (*32*). We perform this registration between a set of EM-sensed internal airway points and the medial axis of the airway segmented from the CT scan. To collect the EM-sensed points, we deploy a custom tool composed of a plastic sheath with an embedded 6 DOF tracking coil through the bronchoscope tool channel. Prior to executing the planned intervention, the physician first steers the bronchoscope and this tracking tool through a large number of the patient's airways. This process enables us to collect a large point cloud in the EM-tracker space representing the airways. This point cloud is then registered with the medial axes of the airway segmentation from the CT scan. We combine these two approaches by using the fiducial registration as the initialization of the ICP method.

In our in vivo experiments, we used the root-mean-square error (RMSE) to quantify the improvement in the registration. The RMSE is calculated using the following equation:

$$\text{RMSE} = \sqrt{\frac{\sum_{i=1}^{N}(x_i - y_i)^2}{N}} \tag{1}$$

where x_i is a point in the set of EM-sensed internal airway points and y_i is a point in the set of points defining the medial axis of the segmented airway. Fig. S2 provides the RMSE values for each of our experiments along with an image of the alignment of the two point sets as point-clouds before and after calculating the tree-to-tree registration.

In vivo experimental setup

The in vivo porcine experiments were conducted at the University of North Carolina (UNC) at Chapel Hill under the supervision of a veterinary team from the UNC Division of Comparative Medicine (DCM) using a protocol (ID: 20-091.0) approved by the Institutional Animal Care and Use Committee (IACUC). The studies included two animals of species Yorkshire cross swine (102 kg and 42 kg, both male) provided by DCM. The sex and age of the animals was based on availability and not pre-specified by the investigators. There was no inclusion or exclusion criteria, and all provided animals were used in the study. The animals were not genetically modified by the investigators. The veterinary team anaesthetized the animals using a solution of Telazol, Ketamine, and Xylazine, all at 1 ml/kg. They used inhaled isofluorane for maintenance of anesthesia. The veterinary team performed a tracheotomy to circumvent the porcine upper respiratory anatomy which differs from that of humans and is often difficult to intubate (*33*). The animals were placed on a volume-controlled bellows ventilator (Hallowell EMC Model 2000). We used a positive end-expiratory pressure (PEEP) valve (10 cm H_2O) to prevent lung collapse in the peripheral airways. To minimize residual breathing effort and negate the involuntary coughing reflex, the veterinary team administered paralytic (Rocuronium Bromide 10 mg/mL) via a syringe pump (Medfusion 2010i) at an infusion rate of 10 mL/hr. We acquired a CT scan of the lungs using a Siemens Biograph mCT with 140 kVp, 0.8 pitch, and 1.0 mm slice thickness. The CT scan parameters are similar to those used in a clinical chest CT for procedure planning. The initial CT scan was performed during a breath hold in order to stabilize the anatomy to capture a reference image.

Following segmentation, we randomly sampled targets in the porcine lung representing suspicious nodules for the device to reach. The targets were sampled from manually-placed cuboidal regions corresponding to human-like anatomical regions of the porcine lung, as informed by interventional pulmonologists on our team. Defining these regions ensured that our results were as translatable as possible to human lung anatomy by avoiding the notable differences between human and porcine lung anatomy (see the subsection 'Overview of the porcine animal model'). The deployment stages were then carried out, as described in the main body of the paper. At the end of the procedure the animal was euthanized by the veterinary team.

Ex vivo experimental setup

The ex vivo experiments were conducted at UNC Chapel Hill. The protocol for the ex vivo experiments was identical to the protocol used for the in vivo experiments other than tasks that are specific to the lungs being outside of the body. We intubated the lungs by inserting an endotracheal tube through the trachea and inflated the lungs with a constant airway pressure. The pressure was initially set to 1 psi and adjusted for each lung to compensate for air leaks caused by minor damage to the lung suffered when it was harvested. We attached fiducial markers to the surface of the lung for registration. The CT scan parameters were identical to those used in the in vivo experiments. All deployment steps were performed as was done for the in vivo experiments, with the exception of the use of multiple safe insertion time windows as there is no breathing motion in the ex vivo case.

Manual clinical bronchoscopy study experimental setup

The comparative study was conducted at UNC Chapel Hill. The robot deployments were performed using the system described in section 'Steerable needle robotic platform'. The manual clinical bronchoscopy deployments were performed using a bronchoscope from the same manufacturer as the bronchoscope used in the robot deployments, but using the thinnest model available (Ambu aScope, Slim). This model has a 4.3 mm outer diameter at its widest section and a 1.2 mm inner diameter working channel that is 60 cm in length. Thin bronchoscopes with these technical specifications are commonly used clinically to facilitate access to distal airways. As described in the 'Steerable needle robotic platform' section, we used a slightly thicker 5.5 mm outer diameter bronchoscope for the robot deployments because our aiming device cannot fit in the thinner bronchoscope's working channel. We attached a 6DOF electromagnetic tracking sensor to the distal end of the bronchoscope used for manual deployments, as was done for the bronchoscope used in the robot deployments. To be able to measure the targeting error in the manual deployments, we created a trackable needle by embedding a 5DOF electromagnetic sensor in a superelastic nitinol tube with a 0.69 mm outer diameter and a 0.53 mm inner diameter. We did not laser pattern the needle so that its stiffness was consistent with the stiffness of existing clinical tools used in clinical bronchoscopy. We measured this by comparing the articulation capabilities of the bronchoscope with our manufactured straight needle inside the working channel of the bronchoscope against the bronchoscope's articulation with various clinical tools inside its working channel.

The manual clinical bronchoscopy and robot deployments were performed in identical experimental settings. Prior to each deployment, we prepared an ex vivo lung in the same way described in the section 'Ex vivo experimental setup'. After randomly sampling a target in the lung parenchyma, we randomly chose either the manual approach or robot approach to perform a deployment. If the robot system was selected, we used our motion planning algorithm to generate a three-stage plan for the user to follow. If the manual bronchoscopy was selected, the physician used the pre-operative CT scan to plan their deployment, just as is done in a real

clinical setting. During both the manual and robot deployments, our visual user interface was provided to the operator showing four views: the 3D segmented anatomy and sagittal, transverse, and frontal slice views of the CT scan, with the location of the tracked bronchoscope in reference to the target shown in the views (Fig. S3). These four views are commonly used in commercial navigational bronchoscopy systems. During a manual deployment, the physician was permitted to use the CT scanner both prior to deploying the needle and after needle insertion to evaluate their desired positioning relative to the target. The physician was given the option to reposition the bronchoscope or to retract the needle and re-insert based on the information from the CT scan. During an autonomous robot deployment, the user was not permitted to use the CT scanner to modify their bronchoscope positioning or needle deployment. After each needle deployment, a CT scan was acquired to identify whether the needle had collided with any obstacles. Following the post-operative CT scan, the deployed system was retracted and a new target was sampled. The robot and manual deployments never attempted to reach the same target. This was done to avoid biasing the results of the second operator from changes in tissue integrity, such as needle tracks, created by the first operator.

For both the manual and robot deployments, the error of the tracked needle tip with respect to the pre-operatively selected target was measured using the Euclidean distance between the coordinates in 3D space. The length of the manual and robot deployments was measured as the distance the needle travelled in tissue after exiting the airway wall.

Autonomous needle steering

Once the start pose of the steerable needle is set using the aiming device, the system autonomously steers the needle from its current pose to the target. To do so successfully, the system's first step is to account for the deviation of the current pose from the originally planned start pose of the steerable needle. Although a three-stage plan including plans for the bronchoscope, aiming device, and steerable needle was created at the start of the procedure, inaccuracies in deployment of the prior stages (bronchoscope, piercing assembly) will result in some error between the planned start pose of the needle trajectory and the current pose of the inserted needle. We address this by sensing the needle tip pose using its embedded EM tracker and replanning a trajectory to the target from this start pose. The motion planner automatically generates a trajectory that connects the real-world start pose of the needle to the target while passing far from critical anatomical obstacles (*11, 12*). The motion planner explicitly avoids obstacles identified and segmented in the patient-specific CT scan, including the bronchial tree, blood vessels, and the pleural boundary. The planner probabilistically generates plans and selects the plan that maximizes safety, which we define as maximizing the distance from obstacles integrated along the needle path (*12*). Creating plans for the steerable needle taking into account surrounding obstacles took under 1 second for all experiments.

Then, the system controls the needle along the planned trajectory, steering safely and accurately until the needle reaches the target. To steer the needle along the planned trajectory, we adapt the controller originally presented by Rucker et al. (*49*) and extended by Ertop et

al. (*27*). We adapt those methods by breaking the trajectory up into a series of insertions with a pre-determined 10 mm arclength. At the end of each segment of insertion, the controller corrects the rotational angle by reorienting the needle tip (using an Extended Kalman Filter (*27*)) to minimize the angular error with respect to the planned trajectory. Each of these insertion segments takes approximately 4 seconds. In the in vivo experiments, one insertion segment was performed during each safe insertion time window, and the controller was then paused between the safe insertion time windows during normal breathing. In the ex vivo experiments, the segments were executed sequentially with no pause as there is no breathing in the ex vivo experiments. Throughout the autonomous needle insertion, the needle tip's pose is displayed to the physician, enabling them to monitor the path of the needle in the segmented anatomy. Other than spreading of needle insertion across multiple safe insertion time windows in the in vivo case, the process of autonomous needle insertion was identical for both our in vivo and ex vivo experiments.

At the end of each insertion, we calculated the error of the steer in electromagnetic tracker space by taking the Euclidean distance between the tracking coil at the tip of the needle and the target. This was done using the equation $E = \|\mathbf{n} - \mathbf{t}\|_2$, where $\mathbf{n} \in \mathbb{R}^3$ is a three-dimensional vector corresponding to the position of the needle, $\mathbf{t} \in \mathbb{R}^3$ is a three-dimensional vector corresponding to the position of the target, and $\|\cdot\|_2$ is the l^2 vector norm.

Overview of the porcine animal model

We used porcine lungs for our in vivo and ex vivo experiments because of the similarities between the porcine and human lung. The similarities in anatomical and histological properties make the porcine lung a good translational model for respiratory medicine (*33*). Although porcine lungs share many properties with human lungs, there are several notable differences. In humans, the interlobular septa between secondary pulmonary lobules are incomplete, allowing for collateral ventilation through the pores of Kohn. The porcine lung does not have these pores, resulting in little to no collateral ventilation between adjacent lobules (*46*). This anatomical difference results in atelectasis forming more readily in the distal lobes, which is especially noticeable when the bronchoscope is obstructing a portion of the airway lumen. This effect limits the depth to which we can safely navigate the bronchoscope in the in vivo porcine lung. This led us to implement the motion planner to favor more proximal piercing sites, but this did not limit our ability to reach the peripheral lung parenchyma. Additional notable differences are that the branching structure of porcine airways is monopodial compared to the bipodial structure of human airways, and the presence of large blood vessels that run adjacent to the main airway branch bilaterally. These blood vessels make it more challenging to pierce into the parenchyma in porcine lungs.

For our ex vivo experiments, a notable limitation of the ex vivo porcine lung model is in the formation of high intensity interlobular obstacles postmortem. The interlobular septa, in which pulmonary veins and lymphatic vessels run, fill with blood and lymphatic fluid postmortem, creating anatomical obstacles that would otherwise not exist in a typical in vivo setting. In humans,

these interlobular septa measure roughly 0.1mm in thickness (*50*). Given this limitation of the ex vivo model, we excluded deployments where the needle path intersected with unsegmented septa greater than 1 mm.

Statistical analysis

Statistical analysis was performed in Python using the Scipy package (version 1.7.0). Unpaired t-tests were used for comparing the values for the lengths and errors in the ex vivo experiments comparing the performance of the robot system and the manual clinical bronchoscopy. We consider $p < 0.05$ to be statistically significant.

REFERENCES AND NOTES

1. Reed, K. B., Majewicz, A., Kallem, V., Alterovitz, R., Goldberg, K., Cowan, N. J., A. M. Okamura, Robot-assisted needle steering, *IEEE Robotics and Automation Magazine* **18**, 35–46 (2011).

2. Amack, S., Rox, M., Mitchell, J., Ertop. T. E., Emerson, M., Kuntz, A., Maldonado, F., Akulian, J. A., Gafford, J., Alterovitz, R., R. J. Webster, Design and control of a compact modular robot for transbronchial lung biopsy, *Medical Imaging 2019: Image-Guided Procedures, Robotic Interventions, and Modeling* **10951**, 17 (2019).

3. T. K. Adebar, J. D. Greer, P. F. Laeseke, G. L. Hwang, A. M. Okamura, Methods for improving the curvature of steerable needles in biological tissue, *IEEE Transactions on Biomedical Engineering* **63**, 1167–1177 (2015).

4. P. J. Swaney, *et al.*, Toward transoral peripheral lung access: Combining continuum robots and steerable needles, *Journal of Medical Robotics Research* **2**, 1750001 (2017).

5. D. Minhas, J. A. Engh, C. N. Riviere, Testing of neurosurgical needle steering via duty-cycled spinning in brain tissue in vitro, *2009 Annual International Conference of the IEEE Engineering in Medicine and Biology Society* pp. 258–261 (2009).

6. J. M. Leipheimer, *et al.*, First-in-human evaluation of a hand-held automated venipuncture device for rapid venous blood draws, *Technology* **7**, 98–107 (2019).

7. I. Fried, *et al.*, Design considerations for a steerable needle robot to maximize reachable lung volume, *IEEE International Conference on Robotics and Automation* pp. 1418–1425 (2021).

8. A. Majewicz, *et al.*, Behavior of tip-steerable needles in ex vivo and in vivo tissue, *IEEE Transactions on Biomedical Engineering* **59**, 2705–2715 (2012).

9. A. Majewicz, A. M. Okamura, Cartesian and joint space teleoperation for nonholonomic steerable needles, *IEEE World Haptics Conference* pp. 395–400 (2013).

10. S. Patil, R. Alterovitz, Interactive motion planning for steerable needles in 3D environments with obstacles, *2010 3rd IEEE RAS & EMBS International Conference on Biomedical Robotics and Biomechatronics* pp. 893–899 (2010).

11. A. Kuntz, L. G. Torres, R. H. Feins, R. J. Webster III, R. Alterovitz, Motion planning for a three-stage multilumen transoral lung access system, *IEEE/RSJ International Conference on Intelligent Robots and Systems* pp. 3255–3261 (2015).

12. Hoelscher, J., Fu, M., Fried, I., Emerson, M., Ertop, T. E., Rox, M., Kuntz, A., Akulian, J. A., Webster, R. J., R. Alterovitz, Backward planning for a multi-stage steerable needle lung robot, *IEEE Robotics and Automation Letters* **6**, 3987–3994 (2021).

13. M. Fu, O. Salzman, R. Alterovitz, Toward certifiable motion planning for medical steerable needles, *Proc. Robotics: Science and Systems* (2021).

14. F. Liu, A. Garriga-Casanovas, R. Secoli, F. Rodriguez y Baena, Fast and adaptive fractal tree-based path planning for programmable bevel tip steerable needles, *IEEE Robotics and Automation Letters* **1**, 601-608 (2016).

15. M. Pinzi, S. Galvan, F. Rodriguez y Baena, The adaptive hermite fractal tree (AHFT): a novel surgical 3d path planning approach with curvature and heading constraints, *International Journal of Computer Assisted Radiology and Surgery* **14**, 659–670 (2019).

16. A. Favaro, L. Cerri, S. Galvan, F. R. Y. Baena, E. De Momi, Automatic optimized 3d path planner for steerable catheters with heuristic search and uncertainty tolerance, *IEEE International Conference on Robotics and Automation* pp. 9–16 (2018).

17. A. Segato, L. Sestini, A. Castellano, E. De Momi, GA3C reinforcement learning for surgical steerable catheter path planning, *IEEE International Conference on Robotics and Automation* pp. 2429–2435 (2020).

18. A. Segato, *et al.*, Inverse reinforcement learning intra-operative path planning for steerable needle, *IEEE Transactions on Biomedical Engineering* **69**, 1995–2005 (2021).

19. R. Secoli, *et al.*, Modular robotic platform for precision neurosurgery with a bio-inspired needle: System overview and first in-vivo deployment, *PLOS ONE* **17**, 1-29 (2022).

20. R. L. Siegel, K. D. Miller, H. E. Fuchs, A. Jemal, Cancer statistics, 2021, *CA: A Cancer Journal for Clinicians* **71**, 7–33 (2021).

21. Howlader N., Noone A. M., Krapcho M., Miller D., Brest A., Yu M., Ruhl J., Tatalovich Z., Mariotto A., Lewis D. R., Chen H. S., Feuer E. J., Cronin K. A., SEER cancer statistics review, 1975-2018, *National Cancer Institute* (2018).

22. J. Bueno, L. Landeras, J. H. Chung, Updated fleischner society guidelines for managing incidental pulmonary nodules: common questions and challenging scenarios, *Radiographics* **38**, 1337–1350 (2018).

23. L. Yarmus, *et al.*, A prospective randomized comparative study of three guided bronchoscopic approaches for investigating pulmonary nodules: the PRECISION-1 study, *Chest* **157**, 694–701 (2020).

24. J. S. W. Memoli, P. J. Nietert, G. A. Silvestri, Meta-analysis of guided bronchoscopy for the evaluation of the pulmonary nodule, *Chest* **142**, 385–393 (2012).

25. D. E. Ost, *et al.*, Diagnostic yield and complications of bronchoscopy for peripheral lung lesions. Results of the AQuIRE registry, *American Journal of Respiratory and Critical Care Medicine* **193**, 68–77 (2016).

26. Rox, M., Emerson, M., Ertop, T. E., Fried, I., Fu, M., Hoelscher, J., Kuntz, A., Granna, J., Mitchell, J., Lester, M., Maldonado, F., Gillaspie, E. A., Akulian, J. A., Alterovitz, R., R. J. Webster, Decoupling steerability from diameter: helical dovetail laser patterning for steerable needles, *IEEE Access* (2020).

27. Ertop, T. E., Emerson, M., Rox, M., Granna, J., Webster, R. J. Maldonado, R., Gillaspie, E. A., Lester, M., Kuntz, A., Rucker, C., Fu, M., Hoelscher, J., Fried, I., R. Alterovitz, Steerable needle trajectory following in the lung: torsional deadband compensation and full pose estimation with 5DOF feedback for needles passing through flexible endoscopes, *Dynamic Systems and Control Conference* **1** (2020). V001T05A003.

28. A. Kuntz, *et al.*, Toward transoral peripheral lung access: Steering bronchoscope-deployed needles through porcine lung tissue, *Hamlyn Symposium on Medical Robotics* **6**, 9–10 (2016).

29. Rox, M., Emerson, M., Ertop, T. E., Fu, M., Fried, I., Hoelscher, J., Kuntz, A., Granna, J., Mitchell, J., Lester, M., Maldonado, F., Gillaspie, E. A., Akulian, J. A., Alterovitz, R., R. J. Webster, An aiming device for steerable needles, *IEEE/ASME International Conference on Advanced Intelligent Mechatronics* **10951**, 37203 (2020).

30. H. D. Kubo, B. C. Hill, Respiration gated radiotherapy treatment: a technical study, *Physics in Medicine and Biology* **41**, 83–91 (1996).

31. M. Fu, A. Kuntz, R. J. Webster, R. Alterovitz, Safe motion planning for steerable needles using cost maps automatically extracted from pulmonary images, *IEEE/RSJ International Conference on Intelligent Robots and Systems* pp. 4942–4949 (2018).

32. P. J. Besl, N. D. McKay, A method for registration of 3-D shapes, *IEEE Transactions on Pattern Analysis and Machine Intelligence* **14**, 239-256 (1992).

33. Judge, E. P., Hughes, J. M. L., Egan, J. J., Maguire, M., Molloy, E. L., S. O'Dea, Anatomy and bronchoscopy of the porcine lung. A model for translational respiratory medicine, *American Journal of Respiratory Cell and Molecular Biology* **51**, 334–343 (2014).

34. J. Puchalski, Robotic bronchoscopy for the diagnosis of peripheral lung nodules: a review, *Current Pulmonology Reports* **10**, 46–52 (2021).

35. Q.-H. Liu, S.-Q. Ben, Y. Xia, K.-P. Wang, H.-D. Huang, Evolution of transbronchial needle aspiration technique, *Journal of Thoracic Disease* **7**, S224 (2015).

36. Fagogenis, G., Mencattelli, M., Machaidze, Z., Rosa, B., Price, K., Wu, F., Weixler, V., Saeed, M., Mayer, J. E., P. E. Dupont, Autonomous robotic intracardiac catheter navigation using haptic vision, *Science Robotics* **4**, eaaw1977 (2019).

37. A. I. Chen, M. L. Balter, T. J. Maguire, M. L. Yarmush, Deep learning robotic guidance for autonomous vascular access, *Nature Machine Intelligence* **2**, 104–115 (2020).

38. Zevallos, N., Harber, E., Patel, K., Gu, Y., Sladick, K., Guyette, F., Weiss, L., Pinsky, M. R., Gomez, H., Galeotti, J., H. Choset, Toward robotically automated femoral vascular access, *International Symposium on Medical Robotics* pp. 1–7 (2021).

39. H. Saeidi, *et al.*, Autonomous robotic laparoscopic surgery for intestinal anastomosis, *Science Robotics* **7**, eabj2908 (2022).

40. Y. Kim, *et al.*, Telerobotic neurovascular interventions with magnetic manipulation, *Science Robotics* **7**, eabg9907 (2022).

41. XACT Robotics Ltd., `https://xactrobotics.com`. Accessed: 2022-11-01.

42. N. Abolhassani, R. V. Patel, M. Moallem, Needle insertion into soft tissue: a survey, *Medical Engineering & Physics* **29**, 413-431 (2007).

43. R. Seifabadi, I. Iordachita, G. Fichtinger, Design of a teleoperated needle steering system for MRI-guided prostate interventions, *IEEE RAS & EMBS International Conference on Biomedical Robotics and Biomechatronics* pp. 793–798 (2012).

44. T. J. Schwehr, *et al.*, Toward targeted therapy in the brain by leveraging screw-tip soft magnetically steerable needles, *Hamlyn Symposium on Medical Robotics* (2022).

45. P. Moreira, S. Patil, R. Alterovitz, S. Misra, Needle steering in biological tissue using ultrasound-based online curvature estimation, *IEEE International Conference on Robotics and Automation* pp. 4368–4373 (2014).

46. M. K. Azad, H. A. Mansy, P. T. Gamage, Geometric features of pig airways using computed tomography, *Physiological Reports* **4**, e12995 (2016).

47. G.-Z. Yang, *et al.*, Medical robotics—regulatory, ethical, and legal considerations for increasing levels of autonomy, *Science Robotics* **2**, eaam8638 (2017).

48. J. M. Fitzpatrick, D. L. G. Hill, C. R. Maurer Jr., Chapter 8: image registration, *Handbook of Medical Imaging Vol 2* pp. 449–514 (2000).

49. Rucker, D. C., Das, J., Gilbert, H. B., Swaney, P. J., Miga, M. I., Sarkar, N., R. J. Webster, Sliding mode control of steerable needles, *IEEE Transactions on Robotics* **29**, 1289–1299 (2013).

50. E.-Y. Kang, P. Grenier, F. Laurent, N. L. Müller, Interlobular septal thickening: patterns at high-resolution computed tomography, *Journal of Thoracic Imaging* **11**, 260–264 (1996).

Acknowledgments: We thank Gregory Grandio, M.D. for his contribution to the manual bronchoscopy experiments. **Funding:** This research was supported in part by the U.S. National Institutes of Health (NIH) under award R01EB024864 and the U.S. National Science Foundation (NSF) under awards 2008475 and 2038855. The content is solely the responsibility of the authors and does not necessarily represent the official views of NIH or NSF. **Author contributions:** R.A. and R.J.W. conceived the project and oversaw all aspects of the research described herein. All six student authors, M.E., T.E.E., I.F., M.F., J.H., and M.R., contributed equally to the overall project. A.K., M.E., T.E.E., I.F., M.F., J.H., M.R., J.A, and Y.L. conducted experiments. A.K., M.E., T.E.E., I.F., M.F., J.H., and M.R. analyzed the data. T.E.E., M.E., and M.R. designed and implemented the controller. M.E., T.E.E., and M.R. designed and built the actuation unit, fabricated fiducials, and designed and fabricated the aiming device and steerable needle. M.F. designed and implemented the segmentation algorithm. A.K., M.F., and J.H. designed and implemented the motion planning algorithm. I.F., M.F. and J.H. designed and implemented the visualization software. M.E., T.E.E., I.F., M.F., J.H., and M.R. implemented the registration software. J.A., E.A.G., Y.L., and F.M. provided clinical insight in the development of the system and the experimental methods. A.K., M.E., T.E.E., I.F., M.F., J.H., M.R., R.J.W., and R.A. wrote the manuscript. All other authors performed critical revisions. **Competing interests:** A.K., R.J.W., and R.A. are inventors on university-owned patents on medical robotic devices incorporating steerable instruments that have been licensed to industry. The authors have no ownership in, no consulting arrangements with, and no other financial interests in a licensee beyond the patent licenses. The other authors declare no competing interests. **Data and materials availability:** The data that support the findings of this study are provided in the main text and graphs in this paper. The source code for the steerable needle planner is freely available via Zenodo with DOI 10.5281/zenodo.8264222 at `https://zenodo.org/record/8264222`.

SUPPLEMENTARY MATERIALS

Autonomous Medical Needle Steering In Vivo

Alan Kuntz[1], Maxwell Emerson[2], Tayfun Efe Ertop[2], Inbar Fried[3], Mengyu Fu[3], Janine Hoelscher[3], Margaret Rox[2], Jason Akulian[4], Erin A. Gillaspie[5], Yueh Z. Lee[6], Fabien Maldonado[5], Robert J. Webster III[2], Ron Alterovitz[3*]
[1]Kahlert School of Computing and Robotics Center, University of Utah; Salt Lake City, UT 84112, USA.
[2]Department of Mechanical Engineering, Vanderbilt University; Nashville, TN 37235, USA.
[3]Department of Computer Science, University of North Carolina at Chapel Hill; Chapel Hill, NC 27599, USA.
[4]Department of Medicine, Division of Pulmonary Diseases and Critical Care Medicine, University of North Carolina School of Medicine; Chapel Hill, NC 27599, USA.
[5]Department of Medicine and Thoracic Surgery, Vanderbilt University Medical Center; Nashville, TN 37232, USA.
[6]Department of Radiology, University of North Carolina School of Medicine; Chapel Hill, NC 27599, USA.

*Corresponding author. Email: ron@cs.unc.edu.

Supplementary Figures S1 - S3

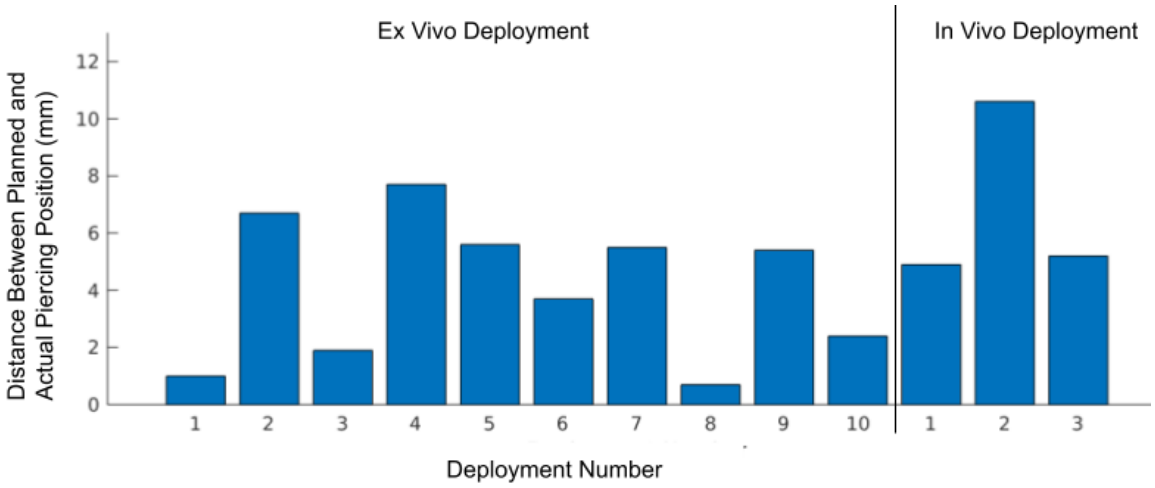

Figure S1: Distance between planned piercing position and actual position reached by the physician.

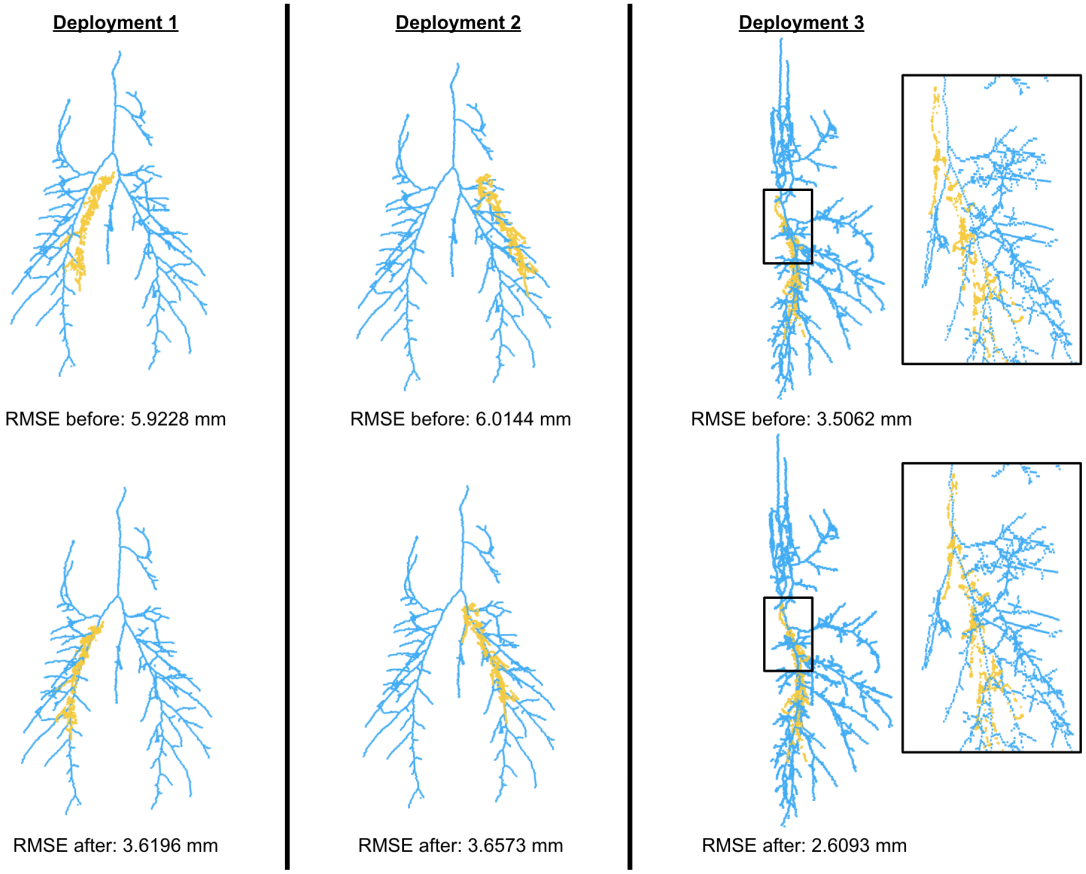

Figure S 2: Tree-to-Tree registration results. For each in vivo deployment, we show the alignment of the bronchial tree skeleton from the segmented CT scan (blue) and the EM tracked bronchoscope positions (yellow) in the coronal plane. We show the alignment before calculating tree-to-tree registration and the alignment after applying the resulting transformation from tree-to-tree registration along with RMSE values. We only segmented the left lung lobe during deployment 3.

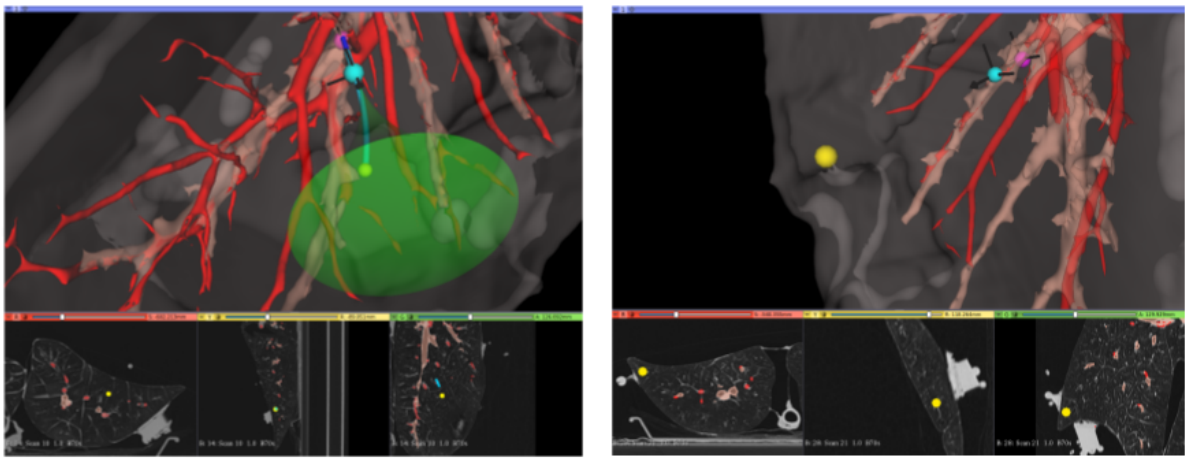

a) Robot Deployment Interface b) Manual Deployment Interface

Figure S 3: User interface display during experiments. In both the automated robot deployments and manual deployments, the physician's user interface displays a 3D visualization including the target (yellow sphere), airways (beige), major blood vessels (red), lung pleura (grey), and the bronchoscope tip (pink). The user interface also displays three perpendicular slice views of the original CT scan. The user can rotate, translate, and zoom into the 3D view and scroll and zoom into the slice views. These four views are commonly used in commercial navigational bronchoscopy systems. a) During automated robot deployments, the visualization also displays a model of the steerable needle's reachable workspace (green funnel shape), the needle's pre-computed motion plan (cyan curve), and the tracked steerable needle's tip (cyan sphere) with respect to the anatomy. b) During manual deployments, the visualization displays the tracked traditional needle's tip (cyan sphere) with respect to the anatomy.